

Fluctuation-dissipation theorem and entanglement dynamics in one-dimensional low-density Jaynes-Cummings Hubbard model after a quench

Qing Li^{1,*}, Jin-Lou Ma^{2,†} and Lei Tan³

¹*School of Jia Yang, Zhejiang Shuren University, Shaoxing, Zhejiang 312028, China*

²*School of Physics and Interdisciplinary Center for Quantum Information, Zhejiang University, Hangzhou 310027, China*

³*Lanzhou Center for Theoretical Physics, Key Laboratory of Theoretical Physics of Gansu Province, Lanzhou University, Lanzhou, Gansu 730000, China*



(Received 19 January 2024; revised 20 May 2024; accepted 31 July 2024; published 19 August 2024)

In one-dimensional low-density Jaynes-Cummings Hubbard (JCH) models [Phys. Rev. E **106**, 064107 (2022)], we proved that the eigenstate thermalization hypothesis (ETH) is valid when the tunneling strength and coupling strength are of the same order. Surprisingly, at the weak tunneling limit, we observed that the entanglement entropy and scaling law of kinetic energy operators also exhibit obvious quantum chaotic properties, this is an unexpected result. To substantiate these findings, we further discuss their nonequilibrium dynamics in this paper. Our analysis reveals that when the model is a weak tunneling limit after the quench and the initial state is an equilibrium state of chaos, the system reaches an equilibrium state. This observation supports the conclusion that the low-density JCH model at the weak tunneling limit is nonintegrable, corroborating our previous results [Phys. Rev. E **106**, 064107 (2022)]. Additionally, by discussing the validity of the fluctuation-dissipation theorem (FDT) and the evolution behavior of entanglement entropy and fidelity, we numerically demonstrate the differences between the one-dimensional low-density JCH model and general nonintegrable systems. Specifically, in the low-density JCH model, when the Hamiltonian after the quench is integrable, the validity of FDT depends on the thermal behavior of the initial Hamiltonian, and a metastable state is observed during the evolution of entanglement entropy. Our research presents an intriguing and unique nonintegrable model, enriching the current understanding of nonintegrable systems.

DOI: [10.1103/PhysRevE.110.024125](https://doi.org/10.1103/PhysRevE.110.024125)

I. INTRODUCTION

A fundamental challenge in physics is how isolated quantum systems evolve on being taken out of equilibrium. For some complex quantum systems, research has found that they inevitably undergo thermalization [1–7], namely, regardless of their initial state, their dynamics all tend to relax to an equilibrium state. This behavior is characteristic of what is known as a quantum chaotic system. However, not all quantum systems exhibit this behavior. For example, quantum integrable systems, which possess a rich symmetry, are incapable of thermalizing [2,8–13].

In 2008, Rigol *et al.* numerically demonstrated that the mechanism of thermalization in quantum chaotic systems is the eigenstate thermalization hypothesis (ETH) [14–16]. When the ETH holds true, for few-body observables, the diagonal matrix elements are smooth functions of energy within the eigenstate of the system, while the off-diagonal elements decrease exponentially with increasing system size. The ETH states that the various eigenstates of a quantum ergodic system can act as thermal ensembles, implying that the relaxation of the system is not strongly dependent on the initial conditions. Although the ETH has been widely applied

in testing across different quantum systems [1,8,10–12,14,17–30], there has been relatively little exploration of thermal properties in coupled cavity systems [31–33]. We use the one-dimensional JCH model within a coupled cavity system as a case study to investigate these properties. In this model, each cavity contains a single two-level atom, where photons interact with the two-level atoms and form an array through photon tunneling between cavities. We have shown that, with the weak tunneling limit, the system is close to the integrable model and cannot achieve thermalization [13]. However, the one-dimensional low-density JCH model exhibits quantum chaotic properties at weak tunneling limits, and the distribution of the majority of matrix elements indicates compliance with the ETH. This finding has sparked significant interest, prompting us to further explore the nonequilibrium dynamics of the low-density JCH model under weak tunneling limits.

The fluctuation-dissipation theorem (FDT) is a pivotal concept in statistical mechanics that describes the relationship between a system's linear response to external perturbations and fluctuations in the equilibrium state [34,35]. Experimentally, the FDT has been found to be fully applicable across various contexts, including Brownian motion [36], electrical currents in resistors [37], quantum gas of light [38], and settings involving cold atomic gases [39–42]. The FDT is one of the indicators of thermal equilibrium state [43,44], but it is difficult to hold in nonequilibrium systems. Therefore, it has been utilized to differentiate between equilibrium and

*Contact author: 601665@zjsru.edu.cn

†Contact author: 0622668@zju.edu.cn

nonequilibrium dynamics [45]. Recent theoretical works suggest that FDT can be extended to a nonequilibrium steady state for fluids [46], and researchers have proposed a theory-independent method to characterize thermalization through the observation of emerging fluctuation-dissipation relations [47]. To explore the relationship between quantum thermalization, fluctuations, and dissipation in isolated quantum systems, we have conducted numerically investigations into the applicability of ETH and FDT within the nonequilibrium dynamics of low-density JCH models. Our findings indicate that the validity of FDT is contingent on the thermal characteristics of the initial Hamiltonian. Furthermore, we note that although the low-density JCH system exhibits chaotic behavior in the weak tunneling limit, its chaotic properties are not entirely analogous to those observed in standard chaotic systems.

The paper is organized as follows. In Sec. II we present the Hamiltonian and the symmetry of the low-density JCH system. Next in Sec. III, we discuss the quench dynamics of the normalized integrable difference. In Sec. IV, the valid of the ETH and FDT are checked with different quench types. In Sec. V, we present the evolution of the half-chain entanglement entropy and fidelity for different initial states. The conclusion is given in Sec. VI.

II. MODEL AND SYMMETRY

In the resonant case, using the operator \hat{U} , the Hamiltonian of a one-dimensional extended JCH model in the rotating frame is ($\hbar = k_B = 1$ throughout this paper) [13]

$$\begin{aligned} \hat{H} = & -J \sum_j^{M-1} (\hat{a}_j^\dagger \hat{a}_{j+1} + \hat{a}_{j+1}^\dagger \hat{a}_j) + g \sum_j^M (\hat{a}_j \hat{\sigma}_j^+ + \hat{a}_j^\dagger \hat{\sigma}_j^-) \\ & + V \sum_j^M \hat{n}_j^\sigma \hat{n}_{j+1}^\sigma, \end{aligned} \quad (1)$$

where $\hat{U} = \exp[i \sum_{j=1}^M (\omega_c \hat{a}_j^\dagger \hat{a}_j + \varepsilon_0 \hat{\sigma}_j^+ \hat{\sigma}_j^-) t]$, the parameters ω_c and ε_0 represent the frequency of the cavity field and the transition frequency of the atom, respectively. The process of rotating frame transformation is shown in Appendix A. In Eq. (1), the symbol $\hat{a}_j^\dagger(\hat{a}_j)$ is creation (annihilation) operator of the photon on site j , $\hat{\sigma}_j^+ = |e\rangle\langle g|$ and $\hat{\sigma}_j^- = |g\rangle\langle e|$ are the spin-flip operators for atoms on site j . The first term in Eq. (1) is the nearest neighbor tunneling of the photons denoted by J , and the second term is the coupling between photons and atoms in the same site with strength g . The last term is the dipole-dipole interaction between atoms. We define the total excitation number operator involved photons and atoms is conservative and equals the number of lattice sites M , i.e., $\langle \hat{N} \rangle = \sum_{j=1}^M \langle \hat{N}_j \rangle = \sum_{j=1}^M (\langle \hat{a}_j^\dagger \hat{a}_j \rangle + \langle \hat{\sigma}_j^+ \hat{\sigma}_j^- \rangle) = M$. But, in this paper, we mainly focus on the case that the JCH model is excited at low-density $\rho \equiv \langle \hat{N} \rangle / M = 1$, where the maximum of photons is taken one in each cavity, so $(\hat{a}_j^\dagger)^2 = (\hat{a}_j)^2 = 0$.

For the open boundary condition, when $V = 0$, the Hamiltonian \hat{H} possesses several symmetries. The first is reflection symmetry, which introduces extra degenerates in the energy spectrum. The second is chiral symmetry, which ensures the

energy spectrum is symmetric about $E = 0$, and the diagonal elements are symmetric with respect to the eigenvalues. The third is particle-hole symmetry, which also induces extra degenerates, and results in no fluctuations in the diagonal elements of the photon occupation operator \hat{n} [48]. When the tunneling strength and the coupling strength are of the same order, the model is nonintegrable, and the average restricted energy gap ratio conforms to the statistics of the Gaussian orthogonal ensemble. However, in the weak tunneling limit, the low-density JCH model displays abnormal thermalization indicators. The average restricted energy gap ratio then exhibits an unusual statistical behavior that does not conform to either Poisson or Gaussian orthogonal ensemble, yet the ETH remains valid.

When $V \neq 0$, the particle-hole symmetry is broken, the Hamiltonian \hat{H} is also nonintegrable with the same order and the ETH is valid, but the ETH is destroyed with the weak tunneling limit.

III. THE RELAXATION DYNAMICS OF THE KINETIC ENERGY OPERATOR

In our previous work, we demonstrated that under the weak tunneling limit, the level spacing distribution of the low-density JCH model does not satisfy either the Poisson or the Wigner-Dyson distributions. However, the finite-size scaling of the matrix elements for the kinetic energy operator of the photons, given by $\hat{T} = \frac{1}{M} \sum_j^M (\hat{a}_j^\dagger \hat{a}_{j+1} + \hat{a}_{j+1}^\dagger \hat{a}_j)$, does satisfy the ETH. This result is surprising and is opposite to that observed in the standard JCH model under the weak tunneling limit. To further investigate this abnormal thermalization indicator, we will discuss the nonequilibrium dynamics of the low-density JCH system. Due to the structure of the model and the ease of detection in experiments, the observables we can discuss are limited to the photon number operator and the photon kinetic energy operator. However, due to particle-hole symmetry, the diagonal elements of the particle number operator (photon number or atomic number) with per site are constant [48], and there is no fluctuation in the dynamic evolution of the particle number operator, thus we do not consider this physical observable. Additionally, considering the dipole-dipole interactions, the particle-hole symmetry is broken, we calculated the evolution of the particle number operator and the kinetic energy operator as observables and found that their results are consistent (see Appendix C). Therefore, we only present the evolution results of the photon's kinetic energy operator in the main text.

The means of nonequilibrium chosen here is quantum quenches. In the following discussion, for the initial Hamiltonian H_i before the quench, we consider two parameter regimes: one where the tunneling and the coupling strengths are of the same order ($J/g = 1$) and another representing weak tunneling limit ($J/g = 0.001$), with dipole-dipole interactions are not considered. There are three parameter regimes of the model used to denote the Hamiltonian H_f after the quench: The tunneling and the coupling strengths are of the same order ($J/g = 1$), the weak tunneling limit ($J/g = 0.001$) without dipole-dipole interactions, and the weak tunneling limit with dipole-dipole interactions ($J/g = 0.001, V/g = 0.5$). The initial state is selected such that the total energy

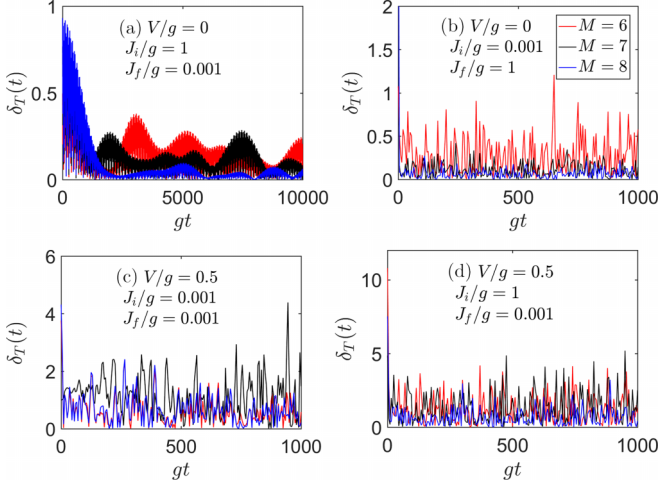


FIG. 1. Time evolution of δ_T after a sudden quench in low-density JCH models with $M = 6, 7, 8$. Results are presented for quenches from $J_i/g = 1$ to $J_f/g = 0.001$ (a), $J_i/g = 0.001$ to $J_f/g = 1$ (b), in these two quenches type, the dipole-dipole interactions cannot be considered for initial and final Hamiltonians. Results are presented for quenches from $J_i/g = 0.001$ to $J_f/g = 0.001$ and $V/g = 0.5$ (c), and $J_i/g = 1$ to $J_f/g = 0.001$ and $V/g = 0.5$ (d), here two quenches type, the initial Hamiltonian still does not include dipole-dipole interactions, but it is considered in the final Hamiltonian.

$E_{\text{tot}} = \langle \phi_i | \hat{H}_f | \phi_i \rangle$ corresponds to that of a canonical ensemble with an inverse temperature $\beta = 0.2$ for different quenches. Here $|\phi_i\rangle$ is a eigenstate state of the initial Hamiltonian H_i , satisfying $E_{\text{tot}} = \text{Tr}\{e^{-\beta \hat{H}_f} \hat{H}_f\} / \text{Tr}\{e^{-\beta \hat{H}_f}\}$. The analysis of different low temperatures revealed no significant impact on the results in Appendix B. We calculate the normalized integrable difference $\delta_T(t) = \frac{|\langle \hat{T}(t) - \bar{T} \rangle|}{\bar{T}}$ [49], which is used to observe the relaxation dynamics of the kinetic energy operator. In this expression, the denominator represents the long-time average of the kinetic energy operator, and the molecule is the absolute difference between its expected value at a certain time and the long-time average of the kinetic energy operator. Figure 1 shows the evolution of δ_T in time for four different types of quenches, which are achieved by varying the tunneling strength of the photons in finite systems. The first two quench types do not consider dipole-dipole interactions in Eq. (1): type (i) transitions from $J_i/g = 1$ to $J_f/g = 0.001$ and type (ii) from $J_i/g = 0.001$ to $J_f/g = 1$. In Figs. 1(a) and 1(b), it is observed that for type (i), the evolution of δ_T towards small amplitude oscillation takes a long time compared to type (ii). However, the amplitude of their oscillations significantly decreases with increasing M , which indicates that the ETH is valid under these two quenches. This is consistent with our previous analysis [48], indicating that both the same order and the weak tunneling limit are nonintegrable. To explore the differences between these two nonintegrable cases, we set them as the Hamiltonian before the quench, while the Hamiltonian after the quench is considered as weak tunneling limit with the dipole-dipole interaction: type (iii) transitions from $J_i/g = 0.001$ to $J_f/g = 0.001$ and $V/g = 0.5$, and type (iv) from $J_i/g = 1$ to

$J_f/g = 0.001$ and $V/g = 0.5$. We have numerically predicted that the Hamiltonian with $J/g = 0.001$ and $V/g = 0.5$ in Eq. (1) is integrable [48], and thus the evolution of δ_T is depended on the Hamiltonian before the quench, as shown in Figs. 1(c) and 1(d). It is evident that the amplitude of the oscillations is relatively large and does not decrease with increasing M . Therefore, for the types (iii) and (iv), the ETH fails. These results are consistent with the ones obtained from the distribution of matrix elements of the observable. It should be noted that for the weak tunneling strength $J/g = 0.001$ mentioned above, the evolution behaviors of δ_T are completely consistent with the weak tunneling strengths $J/g = 0.005$ and $J/g = 0.01$. Therefore, here we only present the evolution result of $J/g = 0.001$, and the following discussion will consider only this parametric case.

IV. FLUCTUATION-DISSIPATION THEOREM

From the point of view of thermal properties, it seems that we cannot clearly find differences between weak tunneling limit and the same order in the absence of dipole-dipole interactions. Therefore, next we focus on the applicability of the FDT in one-dimensional low-density JCH models after a quantum quench. The correlation function $C_{\text{Fluc}}(t)$ is determined by the second moments of a probability distribution for observable O_t , which is defined as [50] $C_{\text{Fluc}}(t) = \frac{O_{t+t'} O_t'}{\langle O_t' \rangle^2}$. Therefore, $C_{\text{Fluc}}(t)$ can be written as

$$C_{\text{Fluc}}(t) \propto \sum_{\substack{\alpha\beta \\ \alpha \neq \beta}} |c_\alpha|^2 |c_\beta|^2 |O_{\alpha\beta}|^2 e^{i(E_\alpha - E_\beta)t}, \quad (2)$$

where E_α and E_β are the eigenvalues ordered in increasing values of energy, and their corresponding eigenstates are $|\alpha\rangle$ and $|\beta\rangle$. $c_\alpha = \langle \alpha | \phi_i \rangle$, $C_{\text{Fluc}}(t)$ explicitly depends on the initial state through c_α . When thermalization occurs, according to the ETH, the correlation function can be defined as [50,51]

$$C_{\text{Appr}}(t) \propto \int_{-\infty}^{+\infty} dw |f(E, w)|^2 e^{iwt}, \quad (3)$$

where $E \equiv \frac{1}{2}(E_\alpha + E_\beta)$, $w \equiv E_\alpha - E_\beta$. $f(E, w)$ is a smooth function of their arguments. Equation (3) implies that $C_{\text{Fluc}}(t)$ does not depend on the initial state under the ETH. Here the function $f(E, w)$ is replaced by the $f_{\text{cg}}(w)$, which is obtained by coarse-graining the off-diagonal values. The discussions of the off-diagonal matrix elements are limited to a narrow energy window centered around the middle of the spectrum, which is defined by the following expression

$$\left(1 - \frac{\epsilon}{2}\right) < \bar{\epsilon} < \left(1 + \frac{\epsilon}{2}\right), \quad (4)$$

Here ϵ is defined as the width of the window, $\bar{\epsilon} = \frac{\epsilon_\alpha + \epsilon_\beta}{2}$, $\epsilon_\alpha = E_\alpha/E_{\text{tot}}$, and $\epsilon_\beta = E_\beta/E_{\text{tot}}$ are reduced eigenvalues, the corresponding eigenstates are $|\alpha\rangle$ and $|\beta\rangle$. The eigenstates are chosen within the energy window of $\epsilon = 0.1$.

For $t \leq 0$, we assume that the quantum state of the system is described by a density matrix $\rho_0 = |\phi_i\rangle\langle\phi_i|$. For $t \geq 0$, this state evolves with the Hamiltonian H_f after a quench, the density matrix at an arbitrary time is $\rho_t = e^{-iH_f t} \rho_0 e^{iH_f t}$. Therefore, the time-dependent expectation value is $O_t \equiv \text{Tr} \rho_t O$, assuming that the perturbation is small, then $O_t = C_{\text{Diss}}(t) O_0$.

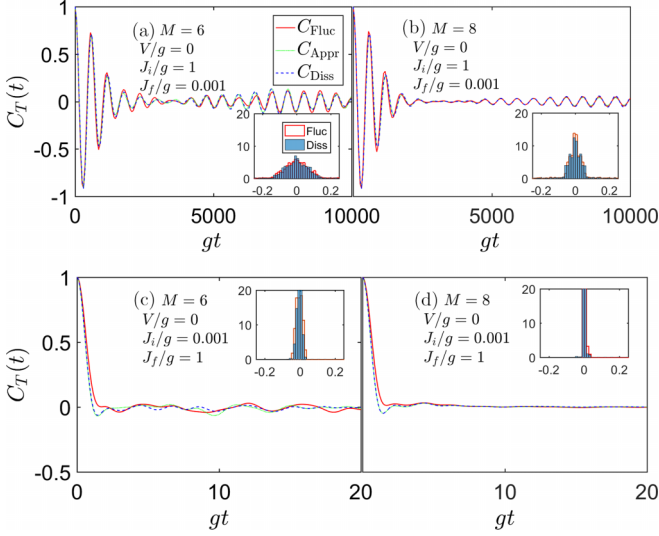


FIG. 2. The time evolution of the correlation functions $C_{\text{Fluc}}(t)$, $C_{\text{Appr}}(t)$, and $C_{\text{Diss}}(t)$ related to the observable \hat{T} . J_i/g and J_f/g represent the tunneling strength of photons before and after the quench, respectively. The insets show normalized histograms of $C_{\text{Fluc}}(t)$ (empty red bars) and $C_{\text{Diss}}(t)$ (filled blue bars) calculated for 2000 data points between $gt = 0$ and 10000 [(a) and (b)] and between $gt = 0$ and 100 [(c) and (d)]. We set $C_{\text{Fluc}}(0) = C_{\text{Appr}}(0) = C_{\text{Diss}}(0) = 1$ [53].

Through Kubo's formula [50,52], $C_{\text{Diss}}(t)$ can be written as

$$C_{\text{Diss}}(t) \propto \sum_{\substack{\alpha\beta \\ \alpha \neq \beta}} \frac{e^{-E_\alpha/T} - e^{-E_\beta/T}}{E_\beta - E_\alpha} |O_{\alpha\beta}|^2 e^{i(E_\alpha - E_\beta)t}. \quad (5)$$

In Fig. 2, the time evolution of three correlation functions is depicted by \hat{T} as physical observables. Figures 2(a) and 2(b) show that for quenches type (i), the three correlation functions initially exhibit significant oscillations, after a long time evolution, the oscillation amplitude gradually decreases and then maintains a small oscillations near zero. This behavior of small oscillations is analogous to the evolution observed in Fig. 1, and it is closely associated with the significant degenerates of the final Hamiltonian. Although it requires an extended period for the evolution to reach dynamic stabilization, and the fluctuations are obvious for much of this duration, the evolution trajectories of the three correlation functions can be more consistent for $M = 8$, suggesting that the DFT and ETH are valid. Moreover, the inset shows that the numerical distribution in the histograms tends to be narrower as the lattice sites increasing. In Figs. 2(c) and 2(d), the three correlation functions rapidly decrease in a short period of time and stabilize near zero for quenches type (ii). In addition, the evolution of the three correlation functions is completely consistent at most times and the distribution of the histograms is more ‘‘sharp’’ as M increases. Through our analysis, we have obtained important information in the low-density JCH model. Although the correlation functions initially exhibit large fluctuations and take a long time to reach relatively small fluctuations when the final Hamiltonian is a weak tunneling limit case, only from the view of the evolution consistency of the three correlation functions, the model under the weak tunneling limit satisfies

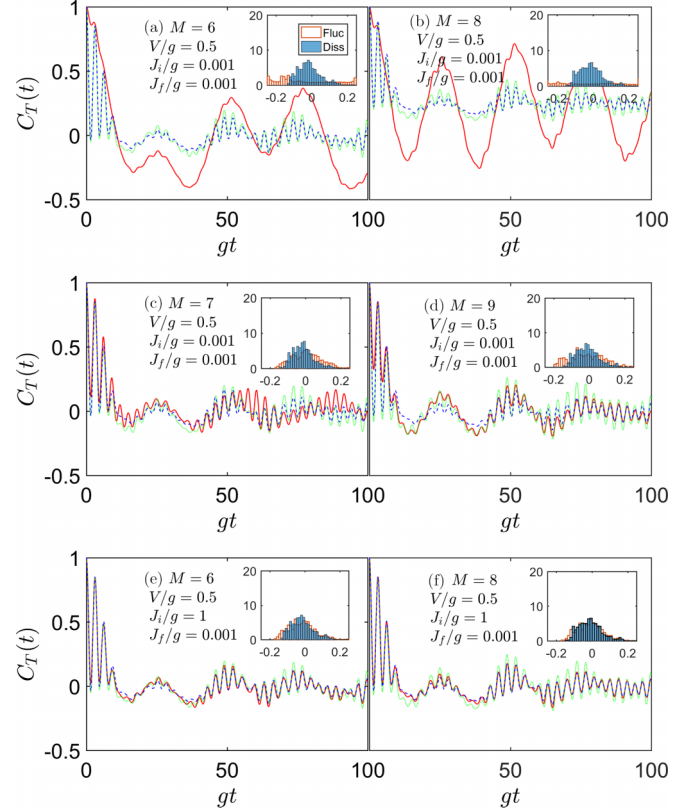


FIG. 3. The time evolution of the correlation functions $C_{\text{Fluc}}(t)$, $C_{\text{Appr}}(t)$, and $C_{\text{Diss}}(t)$ related to the observable \hat{T} with the dipole-dipole interaction term is only considered by final Hamiltonian. The insets show normalized histograms of $C_{\text{Fluc}}(t)$ (empty red bars) and $C_{\text{Diss}}(t)$ (filled blue bars) calculated for 2000 data points between $gt = 0$ and 100.

chaotic behavior. This finding is consistent with the results obtained from finite-size scalings of the matrix elements of \hat{T} .

Next, for quenches type (iii), the time evolutions of three correlation functions are shown in Fig. 3. We find the correlation function C_{Fluc} clearly depends on the parity of lattice number. In Figs. 3(a) and 3(b), the evolution behavior of the correlation function deviates significantly on even sites, indicating that both DFT and ETH are violated. The distribution width of the histogram is larger, and the distribution of C_{Fluc} is more uniform than that of C_{Diss} . Compared to even sites, from Figs. 3(c) and 3(d), the evolution of the correlation function on odd sites are more conventional, the evolution behaviors of the three correlation functions are similar. With increasing M , the C_{Fluc} and C_{Diss} tend to match more and more in the later period of evolution. However, with ongoing evolution time, the deviation between them becomes more and more obvious, thus FDT is invalid. The C_{Fluc} and the C_{Appr} are inconsistent, indicating that ETH is not obeyed. In short, when the Hamiltonian before the quench is a weak tunneling limit, we cannot obtain a very clear result. However, when the Hamiltonian before the quench is standard nonintegrable model, the evolution of the three correlation functions has obvious distribution characteristics. First, the evolution of the three correlation functions is not affected by the parity of lattice number, so we only present the evolution on even sites.

Second, we find that there is always perfect consistency in the evolution of C_{Fluc} and C_{Diss} overall evolution time, but there is a significant deviation from the evolution of C_{Appr} . This indicates that FDT is strongly effective in this case, while ETH is not valid. This outcome is in accordance with the findings obtained from Ref. [53]. Based on the analysis above, we can conclude that when the Hamiltonian after the quench is an integrable model, the evolution of the correlation function strongly depends on the Hamiltonian before the quench. In addition, the results depicted in Fig. 1 indicate that the low-density JCH model with weak tunneling limit is nonintegrable in the absence of dipole-dipole interaction, but when the Hamiltonian after the quench is integrable, the evolution behavior of the correlation function is completely different, depending on whether the initial Hamiltonian is characterized by the weak tunneling limit ($J/g \sim 0.001$) or the standard nonintegrable model ($J/g \sim 1$), as illustrated in Fig. 3.

V. THE EVOLUTION OF THE HALF-CHAIN ENTANGLEMENT ENTROPY AND FIDELITY

Next, we discuss the dynamic evolution of half-chain entanglement entropy and fidelity $|\langle \phi(t)|\phi_i \rangle|^2$ in three initial states, which are all atomic states $|\phi_1\rangle = \prod_i |0, e\rangle_i$, all photon state $|\phi_2\rangle = \prod_i |1, g\rangle_i$ and hybrid state composed of atoms and photons $|\phi_3\rangle = \prod_{i \in \text{odd}} |1, g\rangle_i \otimes \prod_{j \in \text{even}} |0, e\rangle_j$. The Hamiltonians of evolution are $J_f/g = 0.001, V/g = 1$, and $J_f/g = 0.001, V/g = 0.5$.

The half-chain entanglement entropy is defined to be

$$\hat{S}_{M/2}^\alpha = -\text{Tr}_A[\hat{\rho}_A^\alpha \ln \hat{\rho}_A^\alpha], \quad (6)$$

where the system is divided into two subsystems, A and B. When the number of lattice sites is even, the length of both chains A and B is $M/2$. When the number of lattice sites is odd, one chain takes $(M-1)/2$ and the other $(M+1)/2$. So the total Hilbert space is the tensor product $D(M) = D_A \otimes D_B$, where D_A and D_B are the dimensions of the Hilbert space in subsystems A and B, respectively. Then the reduced density matrix for A is given by $\hat{\rho}_A^\alpha = \text{Tr}_B[|\alpha\rangle\langle\alpha|]$, where Tr_B denotes the partial trace over D_B . For fully random states or ergodic states, the mean von Neumann entanglement entropy is given by the Page value [54,55]

$$\overline{S_{\text{Page}}(A)} = \ln D_A - \frac{D_A}{2D_B}, \quad (7)$$

where the horizontal line represents the random vector average.

Figure 4 shows the time evolution of the entanglement entropy $S(t)$ and the fidelity $F(t)$ under the three parameters of the Hamiltonian for three different initial states in the case of finite size $M = 8$. In Figs. 4(a) and 4(d), the Hamiltonian after the quench is the weak tunneling limit and without dipole-dipole interaction, the evolution of $S(t)$ and $F(t)$ coincides completely for the initial states $|\phi_1\rangle$ and $|\phi_2\rangle$, the reason for the coincides is that the system has particle-hole symmetry. But $S(t)$ grows first and reaches saturation value for $|\phi_3\rangle$. At this point, we find that $F(t)$ approaches 1 when $S(t)$ approaches zero for the initial state $|\phi_3\rangle$. Then, within a very short period of time, $S(t)$ rapidly increases to

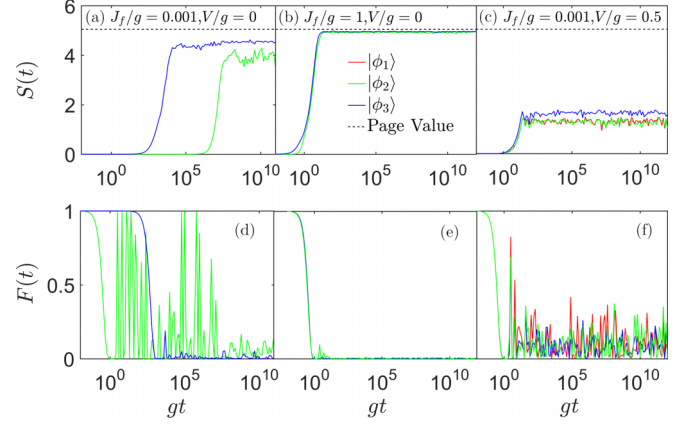


FIG. 4. The time evolution of the entanglement entropy $S(t)$ and the fidelity $F(t)$ for three different parameter cases in the open boundary low-density JCH model. The lines with different colors in the figure represent a quench from different initial states, and the black dashed lines represent the Page value, the number of the lattice sites $M = 8$.

saturation value, while $F(t)$ rapidly decreases to oscillate near zero. More interestingly, for the initial states $|\phi_1\rangle$ and $|\phi_2\rangle$, $S(t)$ appears to rapidly increase from zero to saturation after a long period of time, but $F(t)$ undergoes a long period of oscillation before stabilizing around zero. During this period, $F(t)$ undergoes many processes of recovering from 0 to 1, which indicates that there is still a significant similarity between the state of the system and its initial state at some specific moments, and this similarity is maintained for a long time. Compared to other cases, the time evolution behavior in the low-density JCH model with weak tunneling limits is significantly dependent on the initial state. In addition, in this case, although the model satisfies thermalization behavior, the maximum values of $S(t)$ for the three initial states here cannot reach the Page value. In Figs. 4(b) and 4(e), the final Hamiltonian is completely chaotic, the evolution of $S(t)$ and $F(t)$ for the three initial states are highly consistent. The maximum value of $S(t)$ is very close to the Page value and $F(t)$ decreases to zero, which indicate that the system is chaotic and can thermalize. The final Hamiltonian in Figs. 4(c) and 4(f) is a weak tunneling limit model with dipole-dipole interaction, which is integrable. For the three different initial states, the time evolution behavior of $S(t)$ is largely similar, here the maximum value of $S(t)$ strongly deviates from the Page value and $F(t)$ has been experiencing significant oscillations, which are consistent with the characteristic behaviors of an integrable system that cannot thermalize. From Fig. 4, it can be seen that the evolution behaviors of $S(t)$ for the initial states $|\phi_1\rangle$ and $|\phi_2\rangle$ are nearly identical. Therefore, in the following discussion, we only focus on the initial states $|\phi_1\rangle$ and $|\phi_3\rangle$. Figure 5 shows the time evolution of $S(t)$ and $F(t)$ under three different parameters of the low-density JCH model, where the initial state is a fully atomic state $|\phi_1\rangle$. From Figs. 5(a) and 5(d), when the final Hamiltonian is the weak tunneling limit, we find that $S(t)$ increases after a long period of time and $F(t)$ is also continuously restored for the finite size M . However, Fig. 5(g) indicates that for $M = 6, 8$, $S(t)$ grows in a power law over time until it reaches saturation, while for

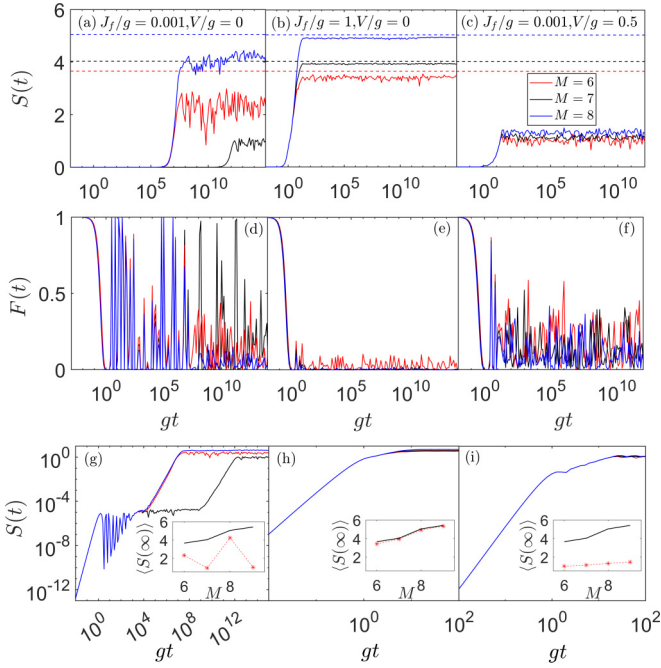


FIG. 5. The time evolution of the entanglement entropy $S(t)$ and the fidelity $F(t)$ for three different parameter cases in the open boundary low-density JCH model. Here the initial state is chosen as the fully atomic state, the lines with different colors in the figure represent different lattice sites and the corresponding Page value. In the insets, black lines are the Page values with the system size increasing. The red dots represent the average entanglement entropy after long times at different system sizes M .

$M = 7$, $S(t)$ remains stable for an intermediate period of time and then increases in a power law until it reaches saturation. Despite exhibiting power-law growth, Fig. 5(a) shows that $S(t)$ cannot reach the Page value for all lattice sites. When the tunneling and coupling strength are of the same order in the final Hamiltonian, which represents a standard nonintegrable model, Fig. 5(b) demonstrates that $S(t)$ increases rapidly in a power law with time and reaches the Page value for different M , which is consistent with the expected behavior of the chaotic system, and as shown in Fig. 5(e), $F(t)$ rapidly drops to zero. In this parameter regime, the rate of change for both $S(t)$ and $F(t)$ is almost unaffected by the number of lattice sites. In Fig. 5(c), we observe that when the final Hamiltonian is the weak tunneling limit with dipole-dipole interaction, an integrable model, the power-law growth behavior of $S(t)$ is identical for different M , and the maximum values of $S(t)$ are very close to each other. However, this maximum values significantly deviate from the Page values. Figure 5(f) also illustrates that the oscillations in $F(t)$ are pronounced, which suggests that the system cannot thermalize. In addition, the inset in Fig. 5(g) reveals that when the final Hamiltonian parameter is $J_f/g = 0.001$, the average saturation value of entanglement entropy after a long time significantly depends on the parity of the system size, deviating from the growth pattern of Page values with increasing size. Conversely, when the final Hamiltonian parameter is $J_f/g = 1$, the inset in Fig. 5(h) demonstrates that the change in average saturation value with size perfectly aligns with the growth pattern of Page val-

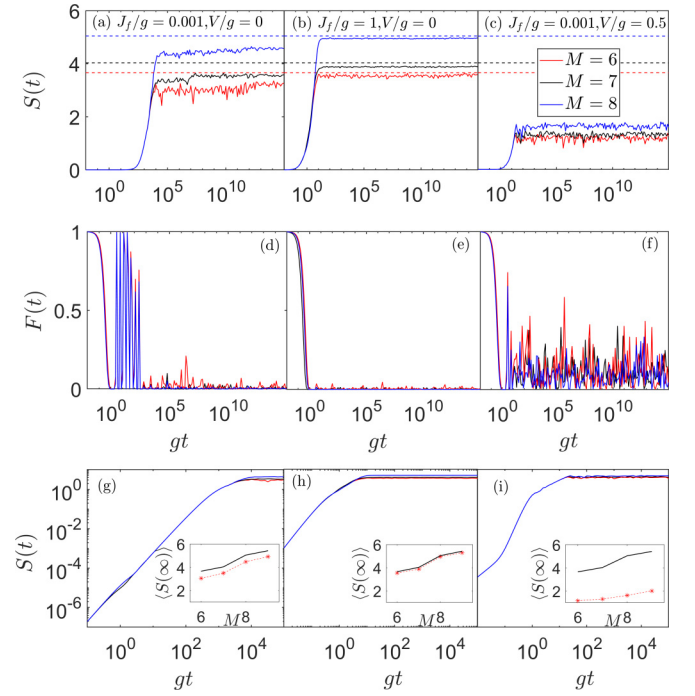


FIG. 6. The time evolution of the entanglement entropy $S(t)$ and the fidelity $F(t)$ for three different parameter cases in the open boundary low-density JCH model. Here, the initial state is chosen as the hybrid state composed of atoms and photons, the lines with different colors in the figure represent different the number of lattice sites and the corresponding Page value. In the insets, black lines are the Page values with the system size increasing. The red dots represent the average entanglement entropy after long times at different system sizes M .

ues. Furthermore, when the final Hamiltonian parameters are $J_f/g = 0.001$ and $V = 0.5$, the inset in Fig. 5(i) indicates a significant deviation in the scaling law of the average saturation value from the Page value.

In Figs. 6(a) and 6(g), when the initial state is a hybrid state composed of atoms and photons, denoted as $|\phi_3\rangle$, and the final Hamiltonian is the weak tunneling limit, the growth trend of $S(t)$ no longer exhibits differences between different finite size M . Furthermore, there is a significant recovery observed in the fidelity $F(t)$, as depicted in Fig. 6(d). In addition, the evolutions of both $S(t)$ and $F(t)$ are identical for the fully atomic state $|\phi_1\rangle$ under other two parameters. From the inset in Figs. 6(g) and 6(h), we find that when the final Hamiltonian parameters are $J_f/g = 0.001$ and $J_f/g = 1$, the average saturation values of entanglement entropy conform to the growth pattern of Page values. However, when the final Hamiltonian has integrable parameters $J_f/g = 0.001$ and $V = 0.5$, the inset in Fig. 6(i) indicates that the scaling law of the average saturation value still deviates significantly from the Page value. The scaling laws of the average saturation values in Figs. 5(g) and 6(g) once again demonstrate that, although ETH is valid for the matrix elements of observable in the low-density JCH model under the weak tunneling limit, the evolution of the system remains dependent on the initial state, a behavior that does not occur in standard chaotic models.

In this section, we also see some notable phenomena. First, when comparing the cases where the final Hamiltonian is the weak tunneling limit and where it is integrable, we note that although the entanglement cannot reach the Page value under the weak tunneling limit, the maximum entanglement value is significantly higher than when the final Hamiltonian is integrable. Second, we also discover that under the weak tunneling limit, both entanglement entropy $S(t)$ and fidelity $F(t)$ take a longer time to reach saturation values. This implies that the initial state information of the system is preserved for an extended period during the evolution.

VI. CONCLUSION

In summary, we have explored the quench dynamics in the one-dimensional low-density JCH model. We have examined the evolution of the normalized integral difference under different quenching mechanisms by adjusting the tunneling strength and increasing the dipole-dipole interaction. The results indicate that when the $J_i/g \sim 1$ and the $J_f/g \sim 0.001$, the fluctuation of the kinetic energy operator decreases significantly with the increasing system sizes, which is consistent with the properties of quantum chaos. However, when the weak tunneling limit is considered as the initial Hamiltonian H_i and compared to standard chaotic parameters as the H_f , the outcomes with the evolution of an integrable H_f are obvious different. For $J_i/g \sim 0.001$, both DFT and ETH are violated. For $J_i/g \sim 1$, the system no longer obeys ETH, but DFT remains valid. Additionally, we have observed that when the initial state is a fully atomic state, the entanglement entropy exhibits a significant metastable state under the weak tunneling limit, which vanishes when the initial state is a hybrid state composed of atoms and photons. Moreover, the behavior of entanglement entropy with the weak tunneling limit also presents anomalies. Compared to the standard chaotic case, the maximum value of entanglement entropy cannot approach the Page value. However, when compared to the integrable case, the entanglement entropy is significantly higher and increases with a power law, which exhibits obvious thermal characteristics. These findings demonstrate the unique thermal properties and rich entanglement dynamics of the low-density JCH model.

ACKNOWLEDGMENT

This work was supported by Zhejiang Shuren University under Grant No. KXJ1422102.

APPENDIX A: ROTATING FRAME TRANSFORMATION

We rewrite the original Hamiltonian \hat{H}' in the following form:

$$\begin{aligned} \hat{H}' &= \sum_j^M (\omega_c \hat{a}_j^\dagger \hat{a}_j + \varepsilon_0 \hat{\sigma}_j^+ \hat{\sigma}_j^-) - J \sum_j^{M-1} (\hat{a}_j^\dagger \hat{a}_{j+1} + \hat{a}_j \hat{a}_{j+1}^\dagger) \\ &\quad + g \sum_j^M (\hat{a}_j \hat{\sigma}_j^+ + \hat{a}_j^\dagger \hat{\sigma}_j^-) + V \sum_j^M \hat{n}_j^\sigma \hat{n}_{j+1}^\sigma \\ &= \hat{H}_{\text{free}} + \hat{H}_{\text{hop}} + \hat{H}_{\text{int}} + \hat{H}_{\text{DDI}}. \end{aligned}$$

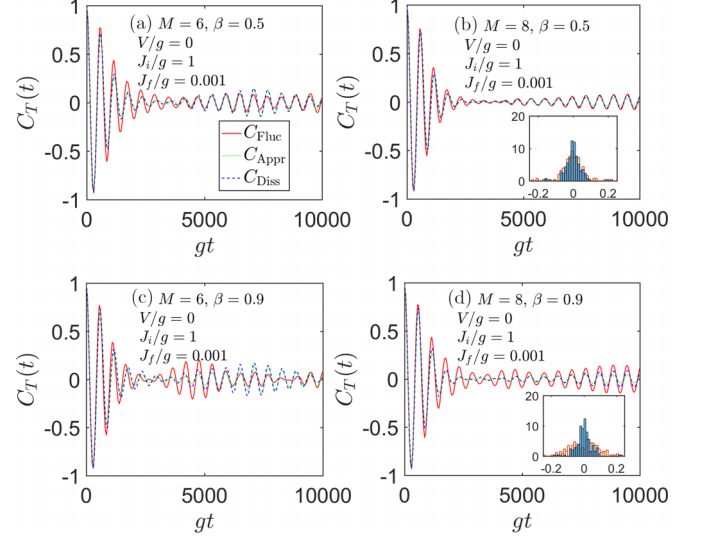


FIG. 7. The time evolution of the correlation functions $C_{\text{Fluc}}(t)$, $C_{\text{Appr}}(t)$, and $C_{\text{Diss}}(t)$ related to the observable \hat{T} . J_i/g and J_f/g represent the tunneling strength of photons before and after the quench, respectively. The insets show normalized histograms of $C_{\text{Fluc}}(t)$ (empty red bars) and $C_{\text{Diss}}(t)$ (filled blue bars) calculated for 2000 data points between $gt = 0$ and 10000. Where we set $C_{\text{Fluc}}(0) = C_{\text{Appr}}(0) = C_{\text{Diss}}(0) = 1$.

Due to $e^A B e^{-A} = B + [A, B] + \frac{1}{2!} [A, [A, B]] + \dots$, then

$$\begin{aligned} \hat{U} \hat{H}' \hat{U}^\dagger &= \hat{U} \hat{H}_{\text{free}} \hat{U}^\dagger + \hat{U} \hat{H}_{\text{hop}} \hat{U}^\dagger + \hat{U} \hat{H}_{\text{int}} \hat{U}^\dagger + \hat{U} \hat{H}_{\text{DDI}} \hat{U}^\dagger \\ &= \omega_c \sum_j^M \hat{a}_j^\dagger \hat{a}_j + \varepsilon_0 \hat{\sigma}_j^+ \hat{\sigma}_j^- - J \sum_j^{M-1} (\hat{a}_j^\dagger \hat{a}_{j+1} + \hat{a}_j \hat{a}_{j+1}^\dagger) \\ &\quad + g \sum_j^M (\hat{a}_j \hat{\sigma}_j^+ + \hat{a}_j^\dagger \hat{\sigma}_j^-) + V \sum_j^M \hat{n}_j^\sigma \hat{n}_{j+1}^\sigma \end{aligned}$$

and $i d\hat{U}/dt \hat{U}^\dagger = -\sum_j^M (\omega_c \hat{a}_j^\dagger \hat{a}_j + \varepsilon_0 \hat{\sigma}_j^+ \hat{\sigma}_j^-)$. Thus, $\hat{U} \hat{H}' \hat{U}^\dagger + i \hbar d\hat{U}/dt \hat{U}^\dagger = \hat{H}$.

APPENDIX B: THE IMPACT OF DIFFERENT TEMPERATURES

In the first part of the paper, we consider the thermodynamic equilibrium state of the initial Hamiltonian as the initial state for the system's evolution. The thermal equilibrium state has an effective temperature which choose the inverse effective temperature $\beta = 0.2$, and the choice of the inverse effective temperature β should ensure that the system still exhibits quantum effects. When $\beta = 0.2$, the effective temperature is $T = 5$. When $\beta = 0$, it implies that the system's temperature tends towards infinity, and such a system loses its quantum effects, so $\beta = 0$ is not an appropriate choice. We have verified that the dynamical evolution results at $\beta = 0.5, 0.9$ are similar to those at $\beta = 0.2$, as show in Fig. 7. Here we only give the evolution of the correlation function for quenches type (i). When $\beta = 0.5$, the evolutionary behavior of the three correlation functions coincides exactly at finite size $M = 8$, which is consistent with the result of the $\beta = 0.2$. When $\beta = 0.9$, the evolution behavior of the three correlation

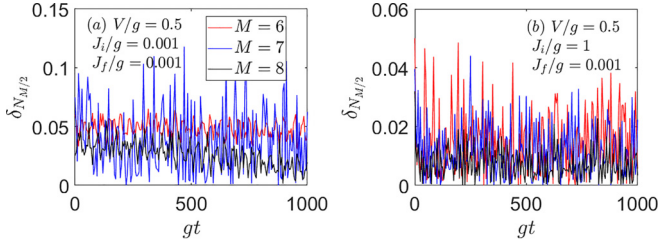


FIG. 8. Time evolution of $\delta_{N_{M/2}}(t)$ (photon) after a sudden quench in low-density JCH models with $M = 6, 7, 8$. Results are presented for quenches from $J_i/g = 0.001$ to $J_f/g = 0.001$ and $V/g = 0.5$ (a), $J_i/g = 1$ to $J_f/g = 0.001$ and $V/g = 0.5$ (b).

functions is not in good agreement, because the temperature of the system is very low in this case, which makes the system more dependent on the finite size effect. However, this does not mean that the evolution behavior of the correlation function at $\beta = 0.9$ contradicts the results we get. As we can see from Figs. 7(c) and 7(d), the evolutionary behavior of the three correlation functions becomes close to each other as the size increasing.

APPENDIX C: THE RELAXATION DYNAMICS OF THE OCCUPATION OPERATOR OF PHOTONS

In our previous considerations, we also looked into focusing on more physical observables. Due to the structure of the model and the ease of detection in experiments, the observables we can discuss are limited to the photon number operator and the photon kinetic energy operator. However, due to particle-hole symmetry, the diagonal elements of the particle number operator (photon or atomic) with per site are constant [48], and there is no fluctuation in the dynamic evolution of the particle number operator, thus we do not consider this physical observable. Additionally, considering the dipole-dipole interactions, the particle-hole symmetry is broken, we calculated the evolution of the particle number operator and the kinetic energy operator as observables and found that their results are consistent, the quench dynamics results of the photon number operator as shown in the Figs. 8 and 9. Figure 8 illustrates the evolution of the normalized integrable difference $\delta_{N_{M/2}}(t) = \frac{|\langle \hat{N}_{M/2}(t) \rangle - \bar{N}_{M/2}|}{\bar{N}_{M/2}}$ after the quench, where $\hat{N}_{M/2}$ is the occupation operator of photons in central site, the dipole-dipole interaction is considered in the final Hamiltonian. Figures 8(a) and 8(b) correspond to the different initial Hamiltonians with reduced tunneling strengths $J_i/g = 0.001$ and $J_i/g = 1$, respectively, it can be observed that $\delta_{N_{M/2}}$ does not decrease with the increase of system size, which indicates that the evolution of particle number difference is related to

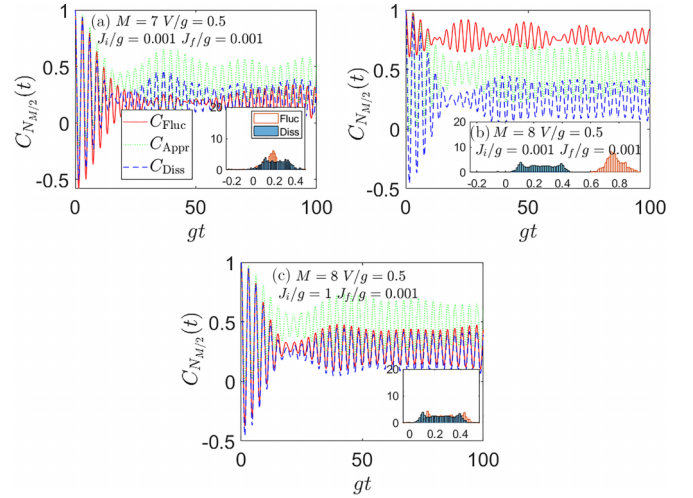


FIG. 9. The time evolution of the correlation functions $C_{\text{Fluc}}(t)$, $C_{\text{Appr}}(t)$, and $C_{\text{Diss}}(t)$ related to the observable $\hat{N}_{M/2}$ with the dipole-dipole interaction term is only considered by final Hamiltonian. The insets show normalized histograms of $C_{\text{Fluc}}(t)$ (empty red bars) and $C_{\text{Diss}}(t)$ (filled blue bars) calculated for 2000 data points between $gt = 0$ and 100.

the initial Hamiltonians in these two cases. This is consistent with the results obtained when the kinetic energy operator is used as an observable, as shown in Figs. 1(c) and 1(d).

Figure 9 presents the time evolution of three correlation functions is depicted by $\hat{N}_{M/2}$ in the final Hamiltonian with the dipole-dipole interaction. Figures 9(a) and 9(b) display the evolution of the $C_{\text{Fluc}}(t)$, $C_{\text{Appr}}(t)$, and $C_{\text{Diss}}(t)$ in the weak tunneling limit for $M = 7$ and $M = 8$, we can see that none of the three correlation functions agree with each other for both sizes, which is consistent with the results obtained using the kinetic energy operator as an observable, as shown in Figs. 3(b) and 3(c). Here, when $M = 8$, the normalized histograms of $C_{\text{Fluc}}(t)$ and $C_{\text{Diss}}(t)$ exhibit divergence in their distribution behavior, yet the width of the distribution remains large, which still aligns with the evolution from an integrable to a chaotic system and is consistent with the results obtained from the kinetic energy operator. In Fig. 9(c), the initial Hamiltonian is a standard chaotic system, hence the evolution of $C_{\text{Fluc}}(t)$ and $C_{\text{Diss}}(t)$ is consistent, while there is a significant deviation from the evolution of $C_{\text{Appr}}(t)$, indicating that the FDT is satisfied but the ETH is violated, which is also completely with the results obtained from the kinetic energy operator, as shown in Fig. 3(f). In summary, the dynamical evolution results are consistent for particle number operator and the kinetic energy operator of the photon.

[1] M. Rigol, *Phys. Rev. A* **80**, 053607 (2009).
 [2] C. Kollath, A. M. Läuchli, and E. Altman, *Phys. Rev. Lett.* **98**, 180601 (2007).
 [3] S. R. Manmana, S. Wessel, R. M. Noack, and A. Muramatsu, *Phys. Rev. Lett.* **98**, 210405 (2007).
 [4] M. C. Bañuls, J. I. Cirac, and M. B. Hastings, *Phys. Rev. Lett.* **106**, 050405 (2011).

[5] M. Rigol, *Phys. Rev. Lett.* **112**, 170601 (2014).
 [6] M. Rigol, *Phys. Rev. Lett.* **116**, 100601 (2016).
 [7] Y. Tang, W. Kao, K.-Y. Li, S. Seo, K. Mallayya, M. Rigol, S. Gopalakrishnan, and B. L. Lev, *Phys. Rev. X* **8**, 021030 (2018).
 [8] M. Rigol, *Phys. Rev. Lett.* **103**, 100403 (2009).
 [9] L. Vidmar and M. Rigol, *J. Stat. Mech.: Theory Exp.* (2016) 064007.

- [10] L. F. Santos and M. Rigol, *Phys. Rev. E* **82**, 031130 (2010).
- [11] R. Steinigeweg, J. Herbrich, and P. Prelovšek, *Phys. Rev. E* **87**, 012118 (2013).
- [12] W. Beugeling, R. Moessner, and M. Haque, *Phys. Rev. E* **89**, 042112 (2014).
- [13] Q. Li, J.-L. Ma, T. Huang, L. Tan, H.-Q. Gu, and W.-M. Liu, *Europhys. Lett.* **134**, 20007 (2021).
- [14] M. Rigol, V. Dunjko, and M. Olshanii, *Nature (London)* **452**, 854 (2008).
- [15] J. M. Deutsch, *Phys. Rev. A* **43**, 2046 (1991).
- [16] M. Srednicki, *Phys. Rev. E* **50**, 888 (1994).
- [17] L. D'Alessio, Y. Kafri, A. Polkovnikov, and M. Rigol, *Adv. Phys.* **65**, 239 (2016).
- [18] J. M. Deutsch, *Rep. Prog. Phys.* **81**, 082001 (2018).
- [19] P. Reimann, *New J. Phys.* **17**, 055025 (2015).
- [20] S. Sorg, L. Vidmar, L. Pollet, and F. Heidrich-Meisner, *Phys. Rev. A* **90**, 033606 (2014).
- [21] D. Jansen, J. Stolpp, L. Vidmar, and F. Heidrich-Meisner, *Phys. Rev. B* **99**, 155130 (2019).
- [22] R. Mondaini, K. R. Fratus, M. Srednicki, and M. Rigol, *Phys. Rev. E* **93**, 032104 (2016).
- [23] H. Kim, T. N. Ikeda, and D. A. Huse, *Phys. Rev. E* **90**, 052105 (2014).
- [24] T. Yoshizawa, E. Iyoda, and T. Sagawa, *Phys. Rev. Lett.* **120**, 200604 (2018).
- [25] W. Beugeling, R. Moessner, and M. Haque, *Phys. Rev. E* **91**, 012144 (2015).
- [26] R. Mondaini and M. Rigol, *Phys. Rev. E* **96**, 012157 (2017).
- [27] R. Steinigeweg, A. Khodja, H. Niemeyer, C. Gogolin, and J. Gemmer, *Phys. Rev. Lett.* **112**, 130403 (2014).
- [28] I. M. Khaymovich, M. Haque, and P. A. McClarty, *Phys. Rev. Lett.* **122**, 070601 (2019).
- [29] M. Mierzejewski and L. Vidmar, *Phys. Rev. Lett.* **124**, 040603 (2020).
- [30] C. Nation and D. Porras, *New J. Phys.* **20**, 103003 (2018).
- [31] Q. Li, J.-L. Ma, and L. Tan, *Phys. Scr.* **96**, 125709 (2021).
- [32] J.-L. Ma, Q. Li, and L. Tan, *Phys. Rev. B* **105**, 165432 (2022).
- [33] J.-L. Ma, B. Liu, Q. Li, Z.-X. Guo, L. Tan, and L. Ying, *Phys. Rev. A* **109**, 033707 (2024).
- [34] H. Nyquist, *Phys. Rev.* **32**, 110 (1928).
- [35] H. B. Callen and T. A. Welton, *Phys. Rev.* **83**, 34 (1951).
- [36] A. Einstein, *Ann. Phys. (Leipzig)* **17**, 549 (1905).
- [37] J. B. Johnson, *Phys. Rev.* **32**, 97 (1928).
- [38] F. E. Öztürk, F. Vewinger, M. Weitz, and J. Schmitt, *Phys. Rev. Lett.* **130**, 033602 (2023).
- [39] J. Esteve, J.-B. Trebbia, T. Schumm, A. Aspect, C. I. Westbrook, and I. Bouchoule, *Phys. Rev. Lett.* **96**, 130403 (2006).
- [40] T. Müller, B. Zimmermann, J. Meineke, J.-P. Brantut, T. Esslinger, and H. Moritz, *Phys. Rev. Lett.* **105**, 040401 (2010).
- [41] C. Sanner, E. J. Su, A. Keshet, R. Gommers, Y.-i. Shin, W. Huang, and W. Ketterle, *Phys. Rev. Lett.* **105**, 040402 (2010).
- [42] K. T. Geier and P. Hauke, *PRX Quantum* **3**, 030308 (2022).
- [43] R. Kubo, M. Toda, and N. Hashitsume, *Statistical Physics II: Nonequilibrium Statistical Mechanics* (Springer, Berlin, 1985), Vol. 31, p. 279.
- [44] G. F. Mazenko, *Nonequilibrium Statistical Mechanics* (Wiley-VCH, Weinheim, 2006).
- [45] J. Kurchan, *Nature (London)* **433**, 222 (2005).
- [46] T. R. Kirkpatrick and D. Belitz, *Phys. Rev. Lett.* **131**, 244001 (2023).
- [47] A. Schuckert and M. Knap, *Phys. Rev. Res.* **2**, 043315 (2020).
- [48] Q. Li, J.-L. Ma, and L. Tan, *Phys. Rev. E* **106**, 064107 (2022).
- [49] M. Rigol and M. Srednicki, *Phys. Rev. Lett.* **108**, 110601 (2012).
- [50] M. Srednicki, *J. Phys. A: Math. Gen.* **32**, 1163 (1999).
- [51] M. Srednicki and F. Stiernelof, *J. Phys. A: Math. Gen.* **29**, 5817 (1996).
- [52] R. Kubo, *J. Phys. Soc. Jpn.* **12**, 570 (1957).
- [53] E. Khatami, G. Pupillo, M. Srednicki, and M. Rigol, *Phys. Rev. Lett.* **111**, 050403 (2013).
- [54] D. N. Page, *Phys. Rev. Lett.* **71**, 1291 (1993).
- [55] A. Russomanno, M. Fava, and R. Fazio, *Phys. Rev. B* **102**, 144302 (2020).